

# Free Energy Surface, Reaction Paths, and Kinetic Isotope Effect of Short-Chain Acyl-CoA Dehydrogenase

Tina D. Poulsen, Mireia Garcia-Viloca, Jiali Gao,\* and Donald G. Truhlar\*

Department of Chemistry and Supercomputing Institute, University of Minnesota,  
Minneapolis, Minnesota 55455

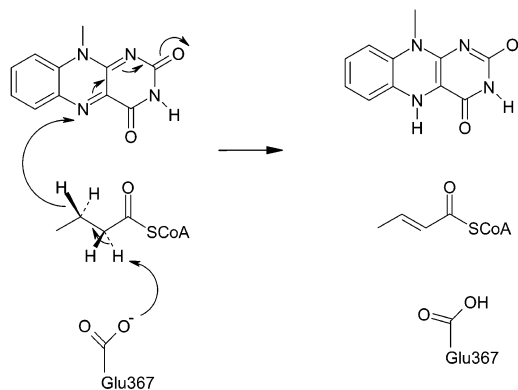
Received: January 27, 2003; In Final Form: May 12, 2003

We have applied molecular dynamics umbrella-sampling simulations and ensemble-averaged variational transition state theory with multidimensional tunneling (EA-VTST/MT) to explore the free energy surface, reaction paths, and dideuterium kinetic isotope effect (KIE) of the  $\beta$ -oxidation of butyryl-coenzyme A by short-chain acyl-CoA dehydrogenase. The potential energy surface is obtained by combined quantum mechanics–molecular mechanics (QM/MM) with specific reaction parameters and a simple valence bond term. The calculations include determination of the potential of mean force (PMF) in both two dimensions (2D) and one dimension (1D) by using the weighted histogram analysis method. The 2D PMF indicates that the hydride transfer is the rate-limiting step of the mechanism, and the 1D PMFs are used to calculate rate constants. We include full molecular dynamics of a 7824-atom reaction zone with stochastic boundary conditions in a first approximation of the quasiclassical rate constant. This first approximation is then corrected by transmission coefficients that account for dynamical recrossing and tunneling. For the calculation of transmission coefficients, the system is divided into a 43-atom primary zone, consisting of atoms directly involved in the enzyme reaction, and a 23 234-atom secondary zone, called the bath. In both approximations considered, the primary zone atoms are allowed to have kinetic energy in all steps. For calculation of the transmission coefficient in the static-secondary-zone (SSZ) approximation, the bath is frozen for each member of an ensemble of transition state configurations and associated reaction paths, which are then averaged, whereas in the equilibrium-secondary-zone (ESZ) approximation 7781 atoms of the bath are fully relaxed (with stochastic boundary conditions) along each reaction path. We found that the SSZ simulations underestimate the KIE, whereas the ESZ simulations overestimate the KIE.

## 1. Introduction

A longstanding goal of enzyme research has been to understand how enzymes facilitate the wide variety of chemical reactions found in biological systems. Important insights into the mechanisms of some enzymes have been obtained from the combination of X-ray crystallography, kinetics, and thermodynamic experiments.<sup>1</sup> However, most enzyme-catalyzed reactions are still not well understood. In this paper, we study one of these reactions, in particular the one catalyzed by acyl-CoA dehydrogenase<sup>2</sup> (ACAD). ACAD catalyzes the first step of the  $\beta$ -oxidation cycle of fatty acids, which is the primary means by which energy stored in adipose tissue is accessed. Deficiency in ACAD, which may be genetic, can lead to serious metabolic disorders or death. Although the mechanism and kinetics of the reaction by ACAD have been extensively investigated experimentally,<sup>2–15</sup> a number of questions remain to be solved. Because acyl-CoA thioesters are oxidized rapidly, it is difficult to experimentally study the properties of the ACAD–substrate complex. Bach, Thorpe, and Dmitrenko<sup>16</sup> have recently summarized the state of knowledge of the mechanism of ACAD by saying that “a number of its critical aspects ... remain cryptic.” Their work involved quantum mechanical calculations on several model systems (consisting of the core reaction and a few of the essential amino acid residues) for the  $\alpha$ -carbonyl proton abstraction step of ACAD, and it opens this enzyme reaction to theoretical study. The present work is the first theoretical study of ACAD including the full enzyme.

## SCHEME 1: First Reaction of the $\beta$ -Oxidation Cycle



ACAD is a flavoprotein, i.e., it operates in conjunction with a flavin cofactor, in particular flavin adenine dinucleotide (FAD), which consists of a tricyclic isoxalloazine moiety (see Scheme 1) connected at N10 to a ribityl side chain, which in turn is diphosphoryladenylated at the 5' position. In most ACADs, including the one studied in this article, the FAD is noncovalently bound to the enzyme and is reduced during the catalytic process.

The oxidation of fatty acids proceeds by first converting the acid to an acyl-CoA, which is a fatty acid thioester conjugate with coenzyme A, i.e.,  $\text{RC(O)-OH} \rightarrow \text{RC(O)-S-CoA}$ , and the acid is transported to a mitochondrion in this activated

thioester state. Then, ACAD catalyzes the first reaction in the oxidation of the thioester, during which FAD is reduced to FADH<sub>2</sub> and the acyl-CoA substrate is oxidized to a *trans*- $\alpha,\beta$ -enoyl-CoA product. This oxidation occurs formally by abstraction of the  $\alpha$ -proton and  $\beta$ -hydride of the substrate. The reaction under study converts FAD to FADH<sup>-</sup> (the one-electron reduced semiquinone anion<sup>2c</sup>).

Various acyl-CoA dehydrogenases are known,<sup>2,13</sup> in particular short-chain (SCAD), medium-chain (MCAD), long-chain, and very long chain acyl-CoA dehydrogenases. Although they are specific for ranges of substrate chain lengths, they exhibit some sequence homology. They also exhibit significant differences; for example one substrate for MCAD is found to be an inhibitor for SCAD.<sup>12</sup> Thus, one should be very cautious about comparing results for SCAD and MCAD. In this paper, we focus on the short-chain acyl-CoA dehydrogenase (EC 1.3.99.2), which was formerly known as butyryl-CoA dehydrogenase. (MCAD (EC 1.3.99.3) was formerly known as general acyl-CoA dehydrogenase.)

At the active site of an ACAD enzyme, a glutamic acid residue (Glu376 for MCAD and Glu367 for SCAD) has been proposed to initiate catalysis by abstracting the substrate  $\alpha$ -hydrogen as H<sup>+</sup>.<sup>10</sup> The first step of the  $\beta$ -oxidation cycle also involves transfer of a hydride ion from the  $\beta$ -carbon to the N5 position of the isoalloxazine ring of the enzyme-bound FAD concomitant with the reduction of the FAD.<sup>6</sup> These steps result in the formation of the one-electron-reduced flavin (FADH<sup>-</sup>) and the corresponding enoyl-CoA product. Conceivably, the removal of two hydrogens can be concerted (separate proton and hydride transfer) or stepwise (Scheme 1). The stepwise mechanism could occur with either proton or hydride transfer first. Furthermore, the concerted mechanism could be either<sup>17</sup> synchronous or asynchronous. (In addition the reaction could also occur by initial  $\alpha$ -proton abstraction and then electron transfer followed by a coupled electron-proton-transfer mechanism—a possibility that we did not simulate.)

Most available experiments are consistent with a concerted mechanism in which proton transfer to Glu precedes hydride transfer to FAD;<sup>2c,6,8,9</sup> however, the experimental situation is not completely clear. Kinetic isotope effects (KIEs) were first recorded for acyl-CoA dehydrogenases in an unpublished 1974 thesis by Murfin<sup>3</sup> on oxidation of hydrocinnamoyl-CoA by MCAD at 276–278 K. (All KIEs discussed in the present paper are H/D.) At low pH, he observed a KIE of 6.9 for substitution at C2 and no KIE for substitution at C3, implying a stepwise mechanism. At high pH, he observed KIEs of 3.5 for 2,2-*d*<sub>2</sub>, 5.8 for 3,3-*d*<sub>2</sub>, and 17 for 2,2,3,3-*d*<sub>4</sub>. A steady-state model showed that this result could be consistent either with a concerted mechanism or with a stepwise mechanism in which (i) the H<sup>+</sup> transfer and H<sup>-</sup> transfer rate constants are the same within a factor of about 2 and (ii) at least one of the steps has a KIE of at least 15. The phenyl ring in hydrocinnamoyl CoA makes it difficult to compare these results to later experiments (or to the results reported here), but nevertheless it provides mechanistic insight. Thus, a primary-size KIE for substitution at C2 could be consistent with a concerted mechanism or a short-lived intermediate that decays at comparable rates to reactant and product but not with a long-lived intermediate that is in equilibrium with reactant.

A 1980 experiment<sup>4</sup> on MCAD with butyryl-CoA substrate at 298 K was interpreted as involving a proton transfer with a KIE of 1.6 followed by rate-determining hydride or hydrogen atom transfer with a KIE of 15–28 for one class of enzyme sites and 48–53 for a second class of sites, with the different

sites resulting from subunit nonequivalence in the tetrameric enzyme and the range for a given site due to pH dependence.

A 1981 unpublished thesis<sup>5</sup> included KIEs for SCAD with butyryl-CoA substrate and obtained 1.2–1.7, 1.5–1.9, and 2.0–2.2 for C2, C3, and C2 + C3 substitution, respectively.

In an experimental paper from 1986,<sup>8</sup> the observed KIEs for the MCAD reaction with butyryl substrate are as large as 28 and seem to indicate that the mechanism is concerted and synchronous because the KIE at 298 K is significant when either the  $\alpha$  or the  $\beta$  hydrogen is isotopically substituted. In a publication 2 years later,<sup>9</sup> one of the original authors and new co-workers stated that details of the kinetic analysis in the 1986 work were hampered by an incomplete appreciation of the mechanism. The new analysis, however, still presented the “puzzling fact” of a significant KIE for a step with no obvious proton/deuteron transfer. Although these authors did not do any additional experiments with only the  $\alpha$  or  $\beta$  hydrogen isotopically substituted, they stated that the new study supported the nature of the isotope effects found in the 1986 paper. They did an experiment on the enzyme with an  $\alpha,\beta$ -(2*R*,3*R*)-dideuterio-substituted substrate at 277.2 K, and, employing the new mechanism, they found a large KIE. Ghisla (personal communication) attributes the difference in the magnitude of the effects in the 1986 and 1988 data primarily to the difference in temperature. In light of this discussion, we will only compare to the 1974, 1980, and 1986 experimental results, but we should keep in mind the possible differences of SCAD and MCAD.

The kinetics of acyl-CoA dehydrogenase are strongly pH dependent. Since both the low pH and high pH forms are reactive, Murfin<sup>3</sup> concluded that the ionizable group is probably not directly involved in the hydrogen-transfer reaction (e.g., that it is probably not the base that abstracts the H<sup>+</sup>), but it could control the reaction rate by affecting the geometry at the active site.

The participation of both proton and hydride transfer in this reaction makes it harder to model than simple proton or hydride transfer reactions. This paper uses recently developed simulation methods<sup>18–21</sup> to explore the possible pathways for the SCAD reaction with butyryl-CoA substrate and a dideuterated butyryl-CoA substrate with the aim of obtaining an improved understanding of the catalysis and kinetics of the dehydrogenation reaction. We employ a semiempirical potential energy surface. The first goal of our calculations was to calculate a two-dimensional potential of mean force<sup>20,21</sup> (2D PMF) as a function of the proton and hydride transfer coordinates to explore the mechanism. Two-dimensional PMFs are far less common in the literature than the corresponding one-dimensional potentials, and it is only recently that 2D PMFs have been applied in quantum mechanical studies of chemical reactions.<sup>22–24</sup> The second goal was to calculate rate constants and a KIE for comparison with the experimental values. For this, we used a recently developed transition state theory scheme<sup>18,19</sup> that includes the effects (such as zero-point energy) of quantizing vibrations and that is based on a transmission coefficient that includes both dynamical recrossing and multidimensional quantum mechanical tunneling.

## 2. Calculations

**2.1. Potential Energy Surface.** In this paper, we employ a combined quantum mechanical–molecular mechanical (QM/MM) potential energy surface in molecular dynamics free energy simulations. In QM/MM calculations, key atoms in the active site of the enzyme are treated by quantum mechanical (QM) methods, and the rest of the system (consisting of the nonpri-

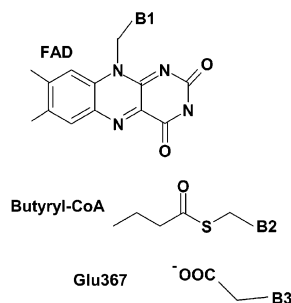


**Figure 1.** Schematic representation of the quantum mechanical region and boundary atoms in acyl-CoA dehydrogenase. The atoms denoted as B1, B2, and B3 are boundary atoms.

mary-system parts of the enzyme, cofactor, substrate, and solvent) is treated by molecular mechanics (MM), i.e., a valence force field augmented by Coulomb interactions between point charges and van der Waals interactions between nonbonded atoms. The boundary between the QM and MM parts is treated with the generalized hybrid orbital (GHO) method.<sup>25</sup> In this method, a set of hybrid orbitals (one active orbital and three auxiliary orbitals) is placed on each boundary atom between the QM and MM fragments. The boundary atoms are part of the quantum mechanical subsystem, but they are also treated partly by molecular mechanics.<sup>25</sup> In principle one should reoptimize the MM parameters for atoms near the boundary,<sup>25</sup> but in this study we use only standard CHARMM<sup>26</sup> parameters at the QM–MM boundary, although we do use modified Lennard-Jones parameters<sup>27</sup> for QM atoms as discussed in section 2.1.2.

For the electronic structure calculations, a total of 55 atoms, including three boundary atoms, are included in the QM part as shown in Figure 1. Since the substrate and the FAD cofactor are fairly large, only parts of them are included in the quantum mechanical subsystem. Furthermore, since the Glu367 takes part in the reaction by abstracting the  $\alpha$ -proton, it is also partly included in the QM part. The system contains three boundary atoms, labeled B1, B2, and B3, which are, respectively, the 1'-C atom of the ribityl chain of the flavin, the C $_{\beta}$  atom of the mercaptoethylamine part of the CoA, and the  $\beta$  carbon of Glu367.

**2.1.1. Gas-Phase Calculations.** The QM method employed in the enzymatic QM/MM calculations is the semiempirical Austin Model 1 (AM1).<sup>28</sup> To investigate the performance of the AM1 calculations for the present enzymatic reaction, we performed calculations on smaller model reactions. These are gas-phase systems that model the species in the active site, and the calculations are performed to calibrate the methods to be employed for the studies in the enzyme. The model reactions are shown in Scheme 2, part a (model of proton-transfer step) and part b (model of hydride-transfer step).

The energy of reaction and barrier height for the two model reactions were determined by including electron correlation at the second-order Møller–Plesset perturbation theory and a polarized, augmented split valence basis set (MP2/6-31+G(d)//HF/6-31+G(d)<sup>29</sup>). In addition we have performed Gaussian-3<sup>30</sup> (G3) calculations for the first model reaction. The GAUSS-IAN98<sup>31</sup> and CHARMM<sup>32</sup> programs were used for these calculations.

The energies of reaction for the two model reactions are shown in Tables 1 and 2. (All values in both tables are based on electronic energies plus nuclear repulsion, without vibrational contributions.) From Table 1, we observe that AM1 underestimates the energy of reaction for the first model reaction (proton transfer). To correct this error of the semiempirical method we used specific reaction parameters (SRP)<sup>33</sup> in the AM1 model.

**TABLE 1: Energies of Reaction (kcal/mol) for the Model Proton-Transfer Reaction Shown in Scheme 2a**

method	$\Delta E$
AM1	1.1
MP2/6-31+G(d)//HF/6-31+G(d)	25.4
G3	18.7
AM1-SRP	19.9

**TABLE 2: Energies of Reaction and Barrier Heights (kcal/mol) for the Hydride-Transfer Reaction Shown in Scheme 2b**

method	$\Delta E$	barrier height
AM1	−30.6	18.4
MP2/6-31+G(d)//HF/6-31+G(d)	−25.4	6.5

These SRP parameters have been developed from the model reaction by only changing parameters for those atoms that are directly involved in the reaction. We found that it is sufficient to modify the AM1 parameters only for the two carboxylate O atoms in the glutamic acid, Glu367, while the rest of the system, including all other oxygen atoms, was described by the standard AM1 model. For these O atoms only the parameter,  $U_{pp}$ , was changed; it was changed from −78.26 to −80.29 eV, a change of 2.6%. The energy of reaction for the first model reaction with these modified parameters is shown in Table 1.

For the second model reaction (hydride transfer), we found that the semiempirical and ab initio energies of reaction agree within  $\sim 5$  kcal/mol (see Table 2). To test the validity of AM1 for the barrier height, we began with a typical transition state structure taken from a preliminary enzyme simulation. With this structure as a starting point, we performed a restrained gas-phase geometry optimization with  $z = z_*$ , where

$$z = r_{\text{CH}} - r_{\text{HN}} \quad (1)$$

is the difference between the distances of the  $\beta$ -hydrogen of the substrate from the  $\beta$ -carbon of butyl CoA ( $r_{\text{CH}}$ ) and from the N5 of FAD ( $r_{\text{HN}}$ ) and  $z_*$  ( $=0.07$  Å) is the value of  $z$  at the transition state, based on a preliminary simulation. A large number of additional geometrical constraints were employed to keep the relative orientation of the cofactor and substrate similar to the orientation in the enzyme simulations, and other geometrical variables were optimized. Table 2 shows barrier heights calculated in this way (with the same constraints) by AM1 and MP2, and it shows that the AM1 barrier is about 12 kcal/mol too high. To correct the AM1 barrier height for the hydride transfer we added a simple valence bond (SVB) correction term given by<sup>34</sup>

$$E_{\text{SVB}} = \frac{1}{2} [M_1(r_{\text{CH}}) + M_2(r_{\text{HN}})] - \frac{1}{2} ([M_1(r_{\text{CH}}) - M_2(r_{\text{HN}})]^2 + 4[V_{12}(r_{\text{CN}})]^2)^{1/2} + \Delta D_{\text{CH}} \quad (2)$$

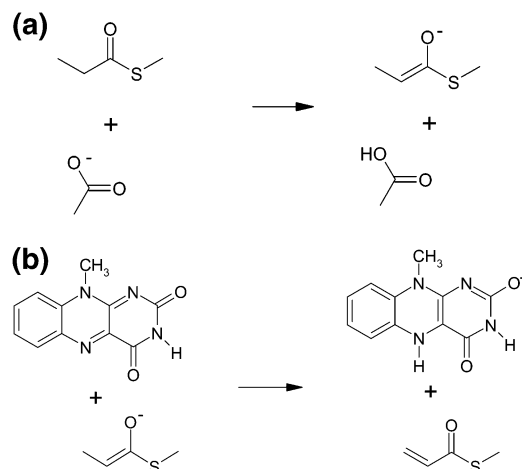
where  $r_{\text{CN}}$  is the distance between the  $\beta$ -carbon of substrate and N5 of FAD, the function  $V_{12}$  is given by

$$V_{12}(r_{\text{CN}}) = D_{\text{CN}} \exp[-\alpha_{12}(r_{\text{CN}} - r_{\text{CN}}^0)] \quad (3)$$

and

$$M(r_{\text{AB}}) = \Delta D_{\text{AB}} (\exp[-2\alpha_{\text{AB}}(r_{\text{AB}} - r_{\text{AB}}^0)] - 2 \exp(-\alpha_{\text{AB}}(r_{\text{AB}} - r_{\text{AB}}^0))) \quad (4)$$

We set the two values of  $\Delta D_{\text{AB}}$  respectively equal to the difference between AM1 and MP2/6-31+G(d) energies for removing

**SCHEME 2: Model Reactions for (a) Proton Transfer and (b) Hydride Transfer**

**TABLE 3: Parameters Employed in the SVB Correction Term<sup>a</sup>**

$\Delta D_{CH}$	$\alpha_{CH}$	$\Delta D_{NH}$	$\alpha_{NH}$	$D_{CN}$	$\alpha_{12}$
5.00	2.17	1.00	2.35	12.0	2.00

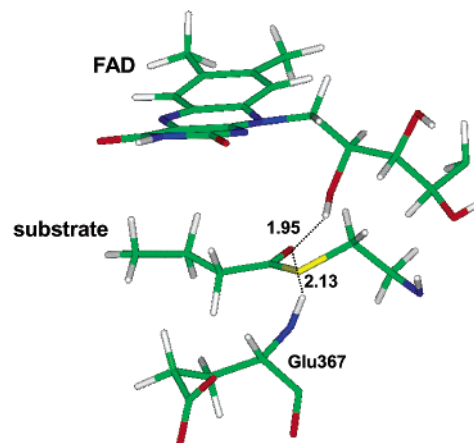
<sup>a</sup> The unit for  $\Delta D_{AB}$  and  $D_{CN}$  is kcal/mol, and the unit for  $\alpha_{AB}$  and  $\alpha_{12}$  is  $\text{\AA}^{-1}$ .

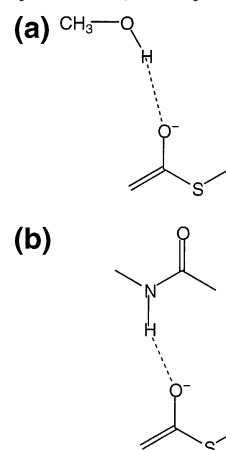
a hydride from the substrate and adding a hydride to FAD (see Scheme 2b), and  $\alpha_{AB}$  ( $AB = CH$  or  $HN$ ) was set equal to  $v_{AB} - (2\pi^2\mu_{AB}/D_{AB})^{1/2}$ , where the stretching vibrational frequency  $v_{AB}$  and  $r_{AB}^0$  are also obtained from MP2/6-31+G(d) calculations. The parameter  $D_{CN}$  is adjusted to account for the difference between the ab initio and semiempirical barrier heights. The bond distance parameters are  $r_{CH}^0 = 1.09 \text{ \AA}$ ,  $r_{NH}^0 = 0.99 \text{ \AA}$ , and  $r_{CN}^0 = 2.73 \text{ \AA}$ . The other parameters are listed in Table 3.

We note that the correction of each of the model reactions does not affect the other one. The modified Glu367 parameters and the SVB term have been included in all the enzyme simulations.

Further work will be required to ascertain the validity of the corrected potential energy surface proposed here, which is a first attempt at obtaining a realistic potential for the ACAD reaction. In this regard, it is instructive to consider a recent study by Field and co-workers<sup>23</sup> on another enzymatic reaction which shows how sensitive the mechanism can be to small changes in the potential and the necessity to consider higher-level corrections. They used a different method for making corrections. First they calculated a 2D free-energy surface at the AM1 level, then they used energy minimizations to calculate potential energy surfaces at both the AM1 and ab initio levels, and finally they added the difference between the two potential energy surfaces as a correction term to each grid point of the free-energy surface. The corrected free-energy surface revealed two possible pathways for the reaction, a stepwise pathway and a concerted one, whereas the uncorrected free energy surface only shows the stepwise pathway. This result should make one cautious about accepting AM1 surfaces without validation or corrections for the specific reaction or a related model reaction.

**2.1.2. Parametrization of Hydrogen Bonds.** From analysis of X-ray structures, it was found that the oxygen of the substrate thioester carbonyl is hydrogen-bonded to the 2'-OH of the ribityl chain of the flavin and the backbone amide N-H of Glu376 (MCAD) or Glu367 (SCAD), which potentially stabilizes the transition state in which the carbonyl group is becoming an enolate anion.<sup>14</sup> These hydrogen bonds are shown in Figure


**Figure 2.** Critical hydrogen bonds for the reaction. Distances are given in  $\text{\AA}$ .

**CHART 1: Model Systems for the Hydrogen Bond Calculations: (a) System H1; (b) System H2**


2. Disruption of the 2'-OH hydrogen bond leads to a substantial transition state destabilization of  $\sim 9 \text{ kcal/mol}$ .<sup>14</sup> Therefore, the flavin cofactor ribitol group is directly involved in the catalysis.

In the enzyme simulations these hydrogen bonds are described as interactions between the QM and MM subsystems since the carbonyl group is included in the QM part, whereas the two hydrogen bond donors are not. To test the quality of this QM/MM description, we have performed a set of model calculations, where we computed the hydrogen bond strength for the two hydrogen bonding interactions noted above. For these systems, Hartree-Fock (HF/6-31G(d)),<sup>29</sup> reduced-order Gaussian-3 (G3-(MP2)),<sup>35</sup> and semiempirical QM/MM energy and geometry calculations have been performed on the hydrogen-bonded systems as well as on the separate monomers.

The calculated hydrogen bond strengths and selected geometrical parameters for the systems in Chart 1a,b are given in Table 4. From the table, it can be observed that with the standard electrostatic and van der Waals parameters in CHARMM, the AM1/MM energies of these two hydrogen bonds are underestimated. The van der Waals interactions are described by a Lennard-Jones term,

$$E_{\text{vdW}} = \sum_{s=1}^S \sum_{m=1}^M 4\epsilon_{sm} \left[ \left( \frac{\sigma_{sm}}{r_{sm}} \right)^{12} - \left( \frac{\sigma_{sm}}{r_{sm}} \right)^6 \right] \quad (5)$$

Here  $S$  and  $M$  are the total number of MM and QM interaction sites and  $r_{sm}$  is the distance of the QM nucleus,  $m$ , from the MM site,  $s$ . The combination rule for the QM-MM interactions



**TABLE 4: Distances and Energies for the Hydrogen Bonds Shown in Chart 1a,b<sup>a</sup>**

	$r$ (Å)			$\Delta E$ (kcal/mol)		
	HF	G3(MP2)	AM1/MM	HF	G3(MP2)	AM1/MM
3a (CHARMM)	1.74	1.73	1.89	15.6	14.3	13.1
3b (CHARMM)	1.74	1.74	1.89	20.7	19.8	16.8
3a (ref 36)			1.64			14.4
3b (ref 36)			1.53			19.2

<sup>a</sup> For the QM/MM calculations, the source of the Lennard-Jones parameters is indicated in parentheses.

are  $\sigma_{sm} = (\sigma_s + \sigma_m)/2$  and  $\epsilon_{sm} = (\epsilon_s \epsilon_m)^{1/2}$ . In the last two rows of Table 4 we have used the values ( $\sigma_m = 1.179$  Å and  $\epsilon_m = 0.15$  kcal/mol) recommended in ref 36 for the oxygen atom that is the acceptor of the hydrogen bonds. This change makes the hydrogen bonds shorter and consequently also stronger. The AM1/MM calculations with the changed van der Waals parameters yield better agreement with the ab initio hydrogen bond energies although the hydrogen bond distances are underestimated (see Table 4). We experimented with other choices of van der Waals parameters but eventually decided to accept the compromise  $\sigma_m$  and  $\epsilon_m$  values of ref 36 rather than propose new specific reaction parameters. The development of more reliable methods of modeling hydrogen bonds in enzymes would be welcome because the effect of approximate bond lengths on catalytic reaction is hard to gauge.

**2.2. Calculations on the Enzyme.** The full model of the substrate–enzyme system was built from the X-ray structure (Protein Databank file PDB: 1BUC) determined by Djordjevic et al.<sup>37</sup> at 2.5 Å resolution. They obtained the enzyme from bacterial cells, and it is a bacterial analogue of the SCAD from mammalian mitochondria. The crystal includes the FAD cofactor and a pseudosubstrate blocked at the  $\beta$  position to prevent reaction. The crystal structure is for a dimer, but the functional form of the protein is a dimer of dimers (a tetramer).<sup>38</sup> The tetrameric structure was constructed by performing the space group operations of the crystal structure, and the blocked substrate was replaced by butyryl-CoA. In the tetramer used for the simulations, we included FAD and the substrate in only one of the four units.

To solvate the structure, a water sphere of 30 Å radius was superimposed on the protein. This sphere was centered at the center-of-mass position of the QM atoms. Water molecules with distances to any protein atoms or crystal water molecules less than 2.5 Å were deleted, and this was repeated three times with randomly rotated water spheres. Then a molecular dynamics simulation (10 ps) was carried out to relax energetically unfavorable contacts, and the 3-fold cycle of superposition, deletion, and rotation was then repeated to fill in additional cavities generated from the equilibration calculations. The final size of the total system is 23 277 atoms; this includes 98 substrate atoms (including the coenzyme A), 88 cofactor atoms, and 6135 water atoms.

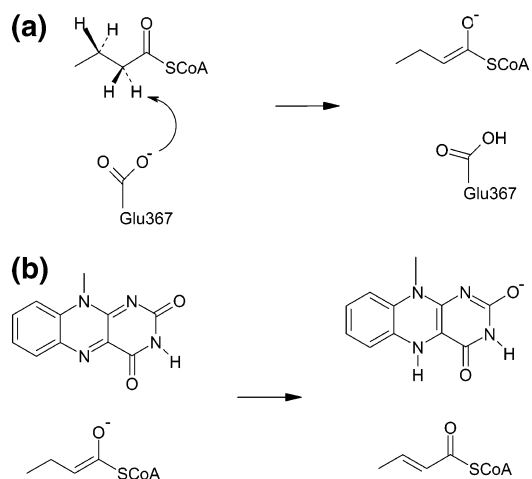
Force field parameters for FAD that are not available in the standard CHARMM force field were set equal to standard CHARMM parameters for closely related atom types. We used a nonbonded cutoff of 12 Å, and the bond lengths and bond angles of all water molecules are constrained by the SHAKE algorithm. All molecular dynamics simulations have been performed at a temperature of 277.2 K, which is the same temperature as two of the kinetics experiments<sup>3,9</sup> to which we compare. A leapfrog Verlet algorithm<sup>39</sup> with a time step of 1 fs is used for all molecular dynamics simulations in this study.

We use stochastic boundary conditions,<sup>40</sup> where the system is divided into three regions: the reaction region; the buffer

region; the reservoir region. The reaction region contains the active center and all atoms within a sphere of radius 24 Å that has its origin at the center of mass of the QM part. The reaction region is treated with Newtonian molecular dynamics. The buffer region extends from 24 to 30 Å. The atoms in the buffer region represent a simplified heat bath and are treated by using the Langevin equations of motion, which impose a friction coefficient and random force on the heavy atoms in this region; the motion of atoms in the buffer region is further restrained by imposing a harmonic restoring force to keep them close to their average positions and to help to maintain the structural integrity of the enzyme. The harmonic force constants are taken as 1.22 kcal mol<sup>-1</sup>Å<sup>-2</sup> for main-chain O atoms, 1.30 kcal mol<sup>-1</sup>Å<sup>-2</sup> for all other main-chain atoms, and 0.73 kcal mol<sup>-1</sup>Å<sup>-2</sup> for side-chain atoms and atoms of water molecules, and the friction constants are 200 ps<sup>-1</sup> for the protein atoms and 62 ps<sup>-1</sup> for the water atoms in the buffer region. The harmonic force constants are gradually scaled to zero at the reaction region boundary. The reservoir region provides a static force field that supplies important electrostatic interactions of protein atoms near the buffer zone–reservoir zone boundary. In addition, a deformable boundary potential<sup>40</sup> is imposed on the water molecules to prevent them from diffusing away. The numbers of atoms in the reaction region, buffer region, and reservoir region are 7824, 6063, and 9390, respectively.

**2.3. Two-Dimensional Free Energy Surface.** To analyze the reaction mechanism, the free energy has been calculated as a function of both  $z_1$  and  $z_2$ , resulting in a two-dimensional potential of mean force (2D PMF). In these simulations, we simultaneously included the reaction coordinates for both the proton transfer and hydride transfer outlined in Scheme 3a,b.

**SCHEME 3: Two Reactions in the Stepwise Mechanism: (a) Proton Transfer; (b) Hydride Transfer**



Each of these reaction coordinates is the difference between the distances of the chemical bonds that are broken and formed. In particular, the reaction coordinate for the proton transfer in Scheme 3a is

$$z_1 = r_{\text{CH}_\alpha} - r_{\text{H}_\alpha\text{O}} \quad (6)$$

where  $r_{\text{CH}_\alpha}$  and  $r_{\text{H}_\alpha\text{O}}$  are distances between the  $\alpha$ -hydrogen and  $\alpha$ -carbon of the substrate and between the  $\alpha$ -hydrogen of the substrate and the side-chain oxygen of Glu367. The reaction coordinate for the hydride transfer in Scheme 3b is

$$z_2 = r_{\text{CH}_\beta} - r_{\text{H}_\beta\text{N}} \quad (7)$$

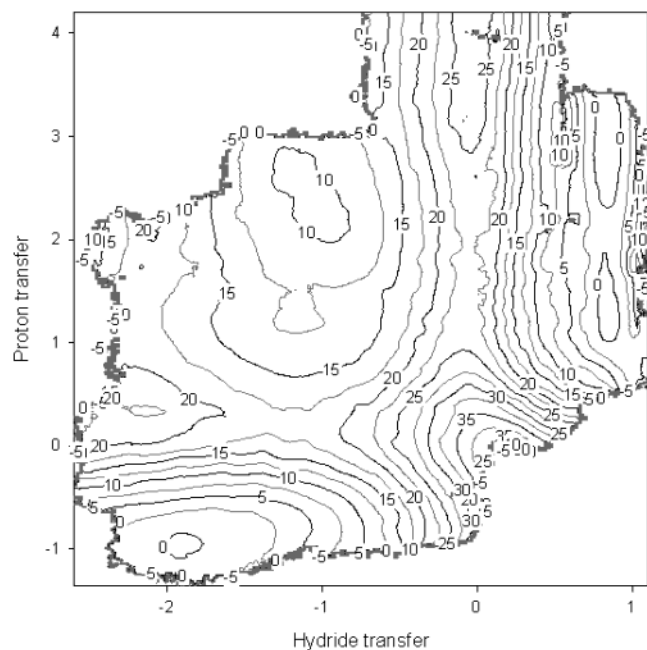


**Figure 3.** Contour plot of the two-dimensional potential of mean force as a function of both the proton transfer and hydride transfer reaction coordinates. The unit of the PMF is kcal/mol, and the unit for the reaction coordinates is Å.

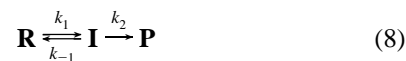
where  $r_{\text{CH}\beta}$  and  $r_{\text{H}\beta\text{N}}$  are distances between the  $\beta$ -hydrogen and  $\beta$ -carbon of the substrate and the  $\beta$ -hydrogen and the N5 atom of FAD.

The two-dimensional free energy surface for the reaction was determined by using the umbrella sampling technique.<sup>41,42</sup> In this method, a series of molecular dynamics simulations are carried out with the addition of a harmonic potential function, centered at a particular point of the 2D grid ( $z_1, z_2$ ). Each of these simulations is called a simulation window, and in each window the potential surface is modified by the harmonic biasing potential to increase the sampling efficiency at ( $z_1, z_2$ ). The distribution function for this effective potential is determined first and then corrected to give the true probability distribution function, from which the free energy is calculated.<sup>41</sup> The PMF was built from the individual simulations by using a weighted histogram analysis method (WHAM).<sup>20,21</sup>

A total of 329 two-dimensional windows were used to build the free energy surface; this is sufficient to ensure good coverage and good overlap between adjacent windows. In each window we used the same harmonic umbrella potential for  $z_1$  and  $z_2$ . In practice, we found that using force constants on the order of 40–90 kcal mol<sup>-1</sup> Å<sup>-2</sup> for the harmonic potentials was adequate; the highest force constants were used in the regions around the transition state. In each window the simulations were run for 50 ps after at least 10 ps of equilibration. Including equilibration, more than 20 ns molecular dynamics simulations have been performed, which involved 20 million electronic structure energy and gradient calculations. All umbrella sampling calculations were performed using a locally modified version of the CHARMM program<sup>32</sup> that has been changed to sample two independent reaction coordinates.

The 2D PMF for the reaction is shown as a contour plot in Figure 3, where the reactant **R** is in the lower left and the product **P** is in the upper right. From this free energy surface, we observe that the reaction occurs in a stepwise manner, with the proton transfer as the first step ( $k_1$ ), followed by hydride transfer ( $k_2$ ); the proton transfer has a free energy barrier height of 18 kcal/mol and a free energy of reaction of 9 kcal/mol in this 2D

representation. We also see that the total free energy barrier height for the overall reaction is 22 kcal/mol, and the free energy of reaction is -1 kcal/mol. If the dip in the free energy profile between the first and second steps is not deep, configurations corresponding to this local minimum would not necessarily be observable as intermediates. Thus, our results could be consistent with an asynchronous, concerted reaction



in which the first step is proton transfer. However, the dip as actually calculated is large enough for an intermediate **I** to be observed, although  $k_{-1}/k_2$  may be close enough to unity that a steady-state rate expression  $k_1 k_2 / (k_{-1} + k_2)$  must be used, with both  $k_1$  and  $k_2$  contributing to the KIEs. If  $k_{-1} \gg k_2$ , then the first step is at equilibrium (with  $K_1$  equal to  $k_1/k_{-1}$ ) and only  $K_1$  and  $k_2$  contribute to the KIE. We note that one cannot calculate rate constants directly from a 2D PMF; transition state theory is directly related to 1D PMFs, but the 2D PMF is useful for understanding the lay of the free energy landscape. We re-emphasize here the importance of the hydrogen bonds discussed in section 2.1.2, which lower the  $\text{p}K_a$  of the  $\alpha$ -H and thus lower the  $\Delta G$  of the first step; this has a profound effect on the reaction profile. Although the predicted mechanism may be sensitive to the quality of the potential energy surface and therefore is not necessarily reliable, the first task in testing potential energy surfaces is understanding what mechanism they predict, and the generation of a 2D PMF proved itself to be a powerful tool in accomplishing this task. We note that although the computation of 2D free energy surfaces is a relatively new field, the effort being devoted to it is already increasing.<sup>20b,20c,21–24,43</sup>

Recently an experimental paper<sup>44</sup> has appeared on nitroalkane oxidase (NAO), which is a very similar enzyme also belonging to the acyl-CoA dehydrogenase super family. The authors of this paper propose that the NAO and ACAD enzymes have evolved such that catalysis by both of them involves a stepwise mechanism in which the first step is proton transfer.

**2.4. One-Dimensional PMFs.** Since the 2D PMF in Figure 3 shows that the  $\beta$ -oxidation reaction of butyryl-CoA takes place via a stepwise mechanism with a discrete intermediate, we also computed the one-dimensional (1D) PMF for each of the reaction steps. As discussed in section 2.5, to calculate kinetic isotope effects we require only the equilibrium constant for the first step (proton transfer), but we require the full one-dimensional (1D) PMF for the hydride-transfer step. In the 1D PMF for the proton-transfer we used  $z_1$  defined in eq 6 as the reaction coordinate, and for the hydride transfer we used  $z_2$  defined in eq 7 as the reaction coordinate. In both cases, we used the structures obtained in the 2D sampling as a starting point for the simulations.

The 1D PMF for the proton transfer and hydride transfer are shown in Figure 4a,b, respectively. In Figure 4b, the zero of energy that we have chosen for the free energy profile is such that the energy of the reactants in Figure 4b equals that of the products of the proton transfer reaction in Figure 4a. The barrier heights for the individual steps as well as the total energy of reaction are in reasonable agreement with those obtained from the two-dimensional PMF. We note that they do not need to be identical because the 1D PMF is not simply a cut through the 2D PMF but rather involves averaging over one more degree of freedom. Additional contributions to the differences may be due to sampling statistics and possibly incomplete equilibration. Because the 2D and 1D free energy barriers are different theoretical quantities, it is significant that the 1D calculations

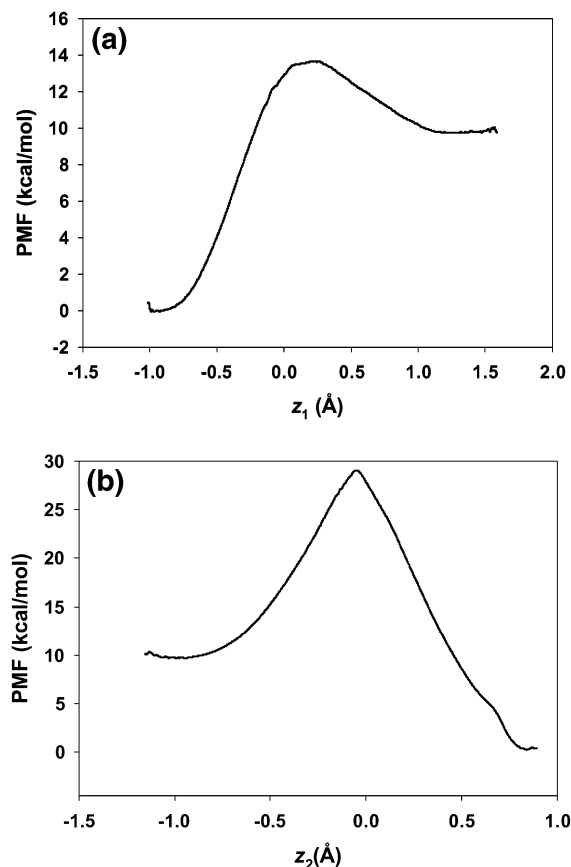


**Figure 4.** Potential of mean force for (a) the proton transfer and (b) the hydride transfer obtained in one-dimensional samplings. These curves treat all vibrations classically (“stage 1, step 1” in the language of ref 18).

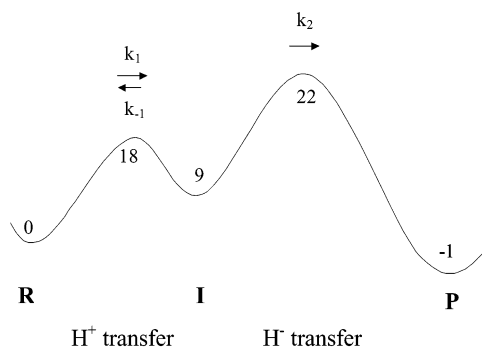


**Figure 5.** Schematic representation of the free energy profile of the two-step mechanism. **R**, **I**, and **P** denote reactant, intermediate, and products. The numerical value at these points and at the two transition states are free energies (in kcal/mol) from the 2D PMF calculation.

confirm that the free energy barrier for the first step is smaller than that for the second step.

**2.5. Reaction Rate Calculations.** To derive an expression for the effective rate constant for the overall reaction, we use the scheme in Figure 5, where **R** and **P** are the reactant and product, respectively, and **I** is the intermediate formed after the proton-transfer step. Using the steady-state approximation, the effective rate constant is given by

$$k_{\text{eff}} = \frac{k_1 k_2}{k_{-1} + k_2} \quad (9)$$

where  $k_1$ ,  $k_{-1}$ , and  $k_2$  are defined in eq 8 and Figure 5. Since

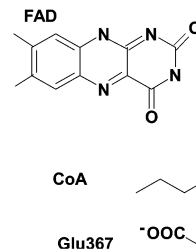


**Figure 6.** Schematic representation of the primary zone.

our calculations yield a  $k_{-1}$  that is much larger than  $k_2$ ,  $k_{\text{eff}}$  is approximately given by

$$k_{\text{eff}} = \frac{k_1 k_2}{k_{-1}} = K_1 k_2 \quad (10)$$

and  $K_1$  is the equilibrium constant for the first step of the reaction.

To study the quantum contributions and the kinetic isotope effect, we consider the effects on  $K_1$  and  $k_2$  separately. The two isotope effects are then multiplied, and the kinetic isotope effect (KIE) on the measurable  $k_{\text{eff}}$  is

$$\frac{k_{\text{HH}}}{k_{\text{DD}}} = \left( \frac{K_1^{\text{HH}}}{K_1^{\text{DD}}} \right) \left( \frac{k_2^{\text{HH}}}{k_2^{\text{DD}}} \right) \quad (11)$$

The calculation of the equilibrium constant  $K_1$  in eq 10 requires quantum mechanical vibrational contributions of the stationary species **R** and **I**, which will be described below. To calculate the rate constant  $k_2$  for the hydride-transfer step we have applied ensemble-averaged variational transition state theory with multidimensional tunneling<sup>18,19</sup> (EA-VTST/MT). This formalism is described in recent papers,<sup>18,45</sup> and most of it is only briefly summarized here, but the ESZ approximation is presented in more detail than in the original<sup>18</sup> paper.

First, a potential of mean force is determined as a function of a predefined reaction coordinate,  $z$ , by using molecular dynamics, which is a classical mechanical simulation (Figure 4b). The hydride-transfer step is represented by the reaction coordinate  $z_2$  in this study (see eq 7). Then the system is partitioned into a primary zone and secondary zone; the latter is called the bath. In this work, the primary zone has 43 atoms and includes parts of the substrate, cofactor, and enzyme. This primary zone is shown in Figure 6; all the other atoms constitute the secondary zone. Then the effect (including zero point energy) of treating vibrations (excluding the degree of freedom corresponding to the reaction coordinate) quantum mechanically is included in the vibrational free energy of the primary zone.<sup>46</sup> These two steps (calculation of the classical mechanical PMF and quantization of primary-zone vibrations) constitute what is called stage 1. The reaction coordinate at which the partially quantized PMF has the highest free energy is the stage-1 quasiclassical variational transition state and is denoted by  $z_*$ . The generalized free energy of activation<sup>47,48</sup> is calculated<sup>18</sup> at this point (neglecting, as before, a small Jacobian term<sup>49</sup>) and is called  $\Delta G_{\text{act}}^{(1)}$  and it yields the stage-1 rate constant (also called the stage-1 quasiclassical rate constant or QC-1) given by

$$k^{(1)}(T) = \frac{k_B T}{h} \exp \left( -\frac{\Delta G_{\text{act}}^{(1)}}{k_B T} \right) \quad (12)$$

where  $k_B$  is Boltzmann's constant,  $h$  is Planck's constant, and  $T$  is the temperature. Note that  $\Delta G_{\text{act}}^{(1)}$  and  $k^{(1)}$  are labeled as quasiclassical quantities to denote that the effect of quantized

vibrations is included, but the reaction coordinate is not quantized. Additional improvements, to be discussed next, produce better approximations to the quasiclassical rate constant by including dynamical recrossing effects, and they also produce higher-level approximations that include quantum mechanical effects (of which the chief one is tunneling) on the reaction coordinate. These improvements (the improved quasiclassical results and also the results that include tunneling) are obtained by multiplying  $k^{(1)}$  by ensemble-averaged transmission coefficients; thus, all the various results include  $k^{(1)}$  as a factor. Since the first step of the calculation of  $k^{(1)}$  is based on molecular dynamics calculations of the full system, all of the approximations to be considered in this paper include the full motion of a very large portion of the enzyme and solvent through their effect on  $k^{(1)}$ .

The transmission coefficients account for recrossing of the stage-1 variational transition state that is defined by constant value  $z_*$  of the predefined reaction coordinate  $z$  (they accomplish this by considering an ensemble average over a sample of individual optimized reaction paths, which are defined below), and they also account for optimized multidimensional tunneling. The transmission coefficient for each transition state configuration is evaluated by either the static-secondary-zone (SSZ) approximation (which involves only stage 2) or the equilibrium-secondary-zone (ESZ) approximation (which also involves stage 3),<sup>18</sup> and the ensemble-averaged transmission coefficient is evaluated by averaging over these individual transmission coefficients. The final expression for the rate constant in either approximation is given by

$$k^{(\sigma)}(T) = \gamma^{(\sigma)} k^{(1)} \quad \sigma = 2 \text{ or } 3 \quad (13)$$

where  $\gamma^{(2)}$  is the full SSZ transmission coefficient and  $\gamma^{(3)}$  is the full ESZ transmission coefficient. Thus  $k^{\text{SSZ}}(T)$  is the same as  $k^{(2)}(T)$ , and  $k^{\text{ESZ}}(T)$  is the same as  $k^{(3)}(T)$ . In the SSZ and ESZ approximations, the transmission coefficients are averaged over transition-state configurations. In practice, one is limited to a finite sample of  $n$  configurations, which may be obtained either by choosing configurations with  $z = z_*$  (in practice we select configurations with  $z$  closest to  $z_*$ ) or (with appropriate accounting for the constraint) by carrying out a molecular dynamics calculation with the constraint of  $z = z_*$ . We have adopted the first approach in this work. In the SSZ ( $\sigma = 2$ ) and ESZ ( $\sigma = 3$ ) approximations, the average transmission coefficient is

$$\gamma^{(\sigma)}(T) = \langle \kappa^{(\sigma)} \Gamma^{(\sigma)} \rangle_{z_*} \approx \left( \sum_{i=1}^n \kappa_i^{(\sigma)} \Gamma_i^{(\sigma)} \right) / n \quad (14)$$

where the brackets  $\langle \dots \rangle_{z_*}$  represent an ensemble average over quasiclassical transition states. Here  $\kappa_i^{(\sigma)}$  and  $\Gamma_i^{(\sigma)}$  ( $\kappa^{(\sigma)}$  and  $\Gamma^{(\sigma)}$  in the notation used with brackets) are the semiclassical transmission coefficient (that accounts mainly for tunneling) and the quasiclassical transmission factor (that accounts for recrossing), respectively, for transition-state configuration  $i$ . By replacing  $\kappa^{(\sigma)} \Gamma^{(\sigma)}$  with  $\Gamma^{(\sigma)}$  in eq 14, we obtain the corresponding SSZ and ESZ quasiclassical results.

The final theoretical estimates of the phenomenological free energy of activation in the SSZ ( $\sigma = 2$ ) and ESZ ( $\sigma = 3$ ) approximations are

$$\Delta G_{\text{act}}^{(\sigma)}(T) = -R \frac{d \ln k^{(\sigma)}}{d(1/T)} = \Delta G_{\text{act}}^{(1)} - RT \ln \gamma^{(\sigma)} \quad (15)$$

where  $R$  is the gas constant.

In both the SSZ and ESZ approximations, the starting point for the calculation of the transmission coefficient is to optimize a saddle point starting from the transition-state configuration  $i$  and determine the minimum energy path, through this saddle point, in mass-scaled coordinates for the primary zone in the static field of transition state configuration  $i$ . We scale<sup>50</sup> all coordinates to a reduced mass of 1 amu. The reaction coordinate for this minimum energy path is denoted by  $s_i$ , which is the signed distance in mass-scaled coordinates along this reaction path. For SSZ calculations, the effective potential for tunneling along path  $s_i$  is equal to the potential energy plus zero point energy of the primary system in the static field of configuration  $i$  of the transition state ensemble (this is the analogue of the vibrationally adiabatic ground-state potential<sup>48,51</sup> potential for gas-phase calculations). For ESZ calculations, the effective potential for tunneling is obtained by adding the free energy of the bath along path  $s_i$ , which yields<sup>18</sup>

$$V_{\text{eff},i}^{(3)}(s) = V_{\text{eff},i}^{(2)}(s) + \Delta G_{\text{bath}}(s) \quad (16)$$

where

$$\Delta G_{\text{bath}}(s) = G_{\text{bath},i}(s) - G_{\text{bath},i}(s_{0,i}) \quad (17)$$

The justification for using the bath free energy in the tunneling transmission is the zero-order canonical mean shape approximation.<sup>52</sup> The changes in bath free energy needed for eq 16 are obtained by employing the free energy perturbation (FEP) method.<sup>53–56</sup> In the FEP calculations, the atoms of the primary zone are held fixed, while molecular dynamics calculations are performed for the atoms of the secondary zone. Since the secondary zone is already equilibrated at transition state configuration  $i$ , which is the starting geometry for the optimized transition structure at  $s = s_{0,i}$ , it is reasonable that we have  $V_{\text{eff},i}^{(3)}(s_{0,i})$  equal to  $V_{\text{eff},i}^{(2)}(s_{0,i})$ .

The quasiclassical SSZ transmission factor is given by

$$\Gamma_i^{(2)} = \exp(-\beta[\Delta G_{T,i}^{(2)}(s_{*,i}^{(2)}) - \Delta G_{T,i}^{(2)}(s_{0,i}^{(2)})]) \quad (18)$$

where  $\beta = 1/k_B T$ ,  $s_{0,i}$  labels the point  $s(z)$ , where  $z = z_*$ , and  $\Delta G_{T,i}^{(2)}$  is the generalized transition state free energy of activation, which has a maximum at  $s = s_{*,i}$ . Note that the zero-temperature limit,  $\Delta G_{T=0,i}^{(2)}$ , of  $\Delta G_{T,i}^{(2)}$  is  $V_{\text{eff},i}^{(2)}$ . The quasiclassical ESZ transmission coefficient is given by

$$\Gamma_i^{(3)} = \exp\{-\beta[\Delta G_{T,i}^{(3)}(s_{*,i}^{(3)}) - \Delta G_{T,i}^{(3)}(s_{0,i}^{(3)})]\} \quad (19)$$

where

$$\Delta G_{T,i}^{(3)}(s) = \Delta G_{T,i}^{(2)}(s) + \Delta G_{\text{bath}}(s) \quad (20)$$

Interpolations required to obtain eq 20 on a finer grid are carried out by a scheme presented elsewhere.<sup>57</sup> The factor  $\kappa_i^{(\sigma)}$  is calculated from<sup>18,48,52</sup>

$$\kappa_i^{(\sigma)} = \int dE P_i^{(\sigma)}(E) \exp[-\beta(E - V_{*,i}^{(\sigma)})] \quad (21)$$

where  $P_i^{(\sigma)}$  is the tunneling probability, and

$$V_{*,i}^{(\sigma)} = V_{\text{eff},i}^{(\sigma)}(s_{*,i}^{(\sigma)}) \quad (22)$$

Both  $V_{*,i}^{(\sigma)}$  and  $s_{*,i}^{(\sigma)}$  depend on the temperature. In this paper we employ the canonical optimized multidimensional tunneling approximation,<sup>58</sup> in which  $P_i^{(\sigma)}$  is evaluated in both the small-curvature tunneling approximation<sup>50,59</sup> and the large-curvature tunneling approximation,<sup>50,60,61</sup> and whichever approximation



yields a larger value for the integral of eq 21 is accepted as the optimized value.

In future discussion, we sometimes replace superscripts (2) and (3) with SSZ and ESZ, respectively.

The quantum mechanical vibrational energy corrections<sup>46</sup> were added to the classical PMF by carrying out generalized normal-mode analyses<sup>50</sup> for 200 configurations in each of the reactant and product windows and for 250 configurations of each of the two transition state windows. The same configurations were used for both hydrogen- and deuterium-transfer reactions. Note that when the effect of quantizing vibrations is added for the perprotio case, we add the free energy of quantized vibrations for the perprotio case and subtract the free energy of classical vibrations for the same case, and when we consider the dideuterated case, we add the free energy of quantized vibrations for the dideuterated case and subtract the free energy of classical vibrations for the dideuterated case. When calculating the generalized normal-mode frequencies, the reaction coordinate was projected out of the Hessian. The calculated vibrational frequencies for the various configurations were averaged over all the configurations that belong to a given bin of width 0.01 Å. The discrete values for the individual bins of the quantum mechanical vibrational energy correction were fitted to a polynomial function of degree five in  $z$  for both hydride and deuteride transfer. The rate constants were calculated from the quantized PMFs by methods described elsewhere.<sup>18,45</sup>

These calculations were performed with the CHARM-MRATE<sup>62</sup> module of CHARMM.<sup>32</sup>

**2.5.1. Equilibrium Isotope Effects for the Proton-Transfer Step.** The equilibrium constant  $K_1$  was computed by including quantized vibrational energy contributions for both the nonsubstituted and the  $\alpha,\beta$ -(2R,3R)-dideuterio-substituted substrates. This calculation involves only the reactant and product of the first step and no transition-state or tunneling information. The reactant and product properties were taken from the simulation in section 2.4, and vibration was quantized as in refs 18 and 46.

The equilibrium constant,  $K_1$ , for the reaction  $\mathbf{R} \rightarrow \mathbf{I}$  is given by

$$K_1 = \exp(-\Delta G_{\mathbf{R} \rightarrow \mathbf{I}}/RT) \quad (23)$$

Here  $\Delta G_{\mathbf{R} \rightarrow \mathbf{I}}$  is the free energy change in going from reactant,  $\mathbf{R}$ , to the intermediate,  $\mathbf{I}$ . We calculated  $\Delta G_{\mathbf{R} \rightarrow \mathbf{I}}$  by correcting the classical free energy of reaction (from the 1D PMF in Figure 4a) for quantum mechanical vibrational contributions at  $\mathbf{R}$  as well as  $\mathbf{I}$  for both isotopes. This gives an isotope effect on  $K_1$  of 1.07.

**2.5.2. Stage-1 Kinetic Isotope Effect for the Hydride-Transfer Step.** In stage 1, quantized vibrational contributions excluding the degree of freedom for the reaction coordinate are included in the rate constant ( $k_2$ ) calculations for both the nonsubstituted and the  $\alpha,\beta$ -(2R,3R)-dideuterio-substituted substrate. Figure 7 shows the quantum mechanical vibrational free energy corrections for the hydride and deuteride transfer as functions of the hydride-transfer reaction coordinate. The inclusion of quantum mechanical vibrational free energy lowers the free energy of activation  $\Delta G_{\text{act}}^{(1)}$  to 15.4 and 16.1 kcal/mol for the hydride and deuteride transfer reactions, respectively. This gives a preliminary KIE of 3.52 for  $k_2$ . The displacement from the classical transition state location due to the inclusion of quantized vibrations in the vibrational free energy is less than 0.01 Å in both cases. The variational transition state is located at  $z_*$  = -0.055 Å.

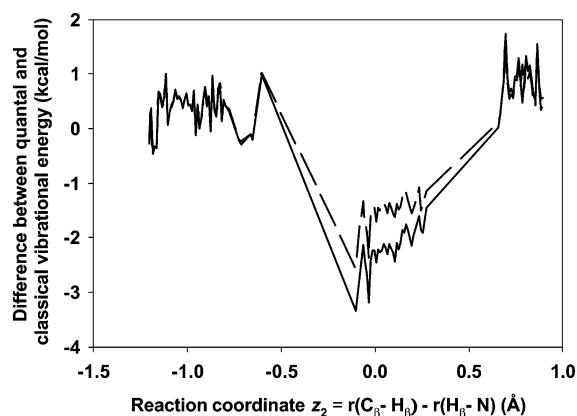


**Figure 7.** Quantum mechanical correction to vibrational free energy for hydride (solid line) and deuteride (dashed line) transfers. The energy is zeroed at the reactant.

**TABLE 5: Computed Transmission Coefficients for the Protio and Deuterio Isotopes Using the Static-Secondary-Zone Approximation Averaged over 15 Configurations<sup>a</sup>**

isotope	$\Gamma^{\text{SSZ}}$	$\kappa^{\text{SSZ}}$	$\gamma^{\text{SSZ}}$
HH	0.36(0.3)	3.5(2)	1.9(2)
DD	0.40(0.3)	3.0(1)	1.6(2)

<sup>a</sup> Values in parentheses are root-mean-square deviations from the mean.

**2.5.3. Tunneling Contributions to the SSZ Kinetic Isotope Effect.** From the quasiclassical stage-1 calculation above, we chose an ensemble of 15 secondary-zone configurations that are closest to  $z_*$  for calculations of the SSZ transmission coefficients using the frozen-bath approximation, in particular the quasiclassical SSZ transmission coefficient that accounts for recrossing and the tunneling SSZ transmission coefficient that accounts for quantum effects on reaction coordinate motion. The 15 configurations are within the interval  $z_* \pm 0.015$  Å (where  $z_*$  is specified in section 2.5.2), and they are at least 0.6 ps apart. The 15 transition state configurations were obtained from an umbrella sampling simulation, spanning 100 ps, which yields a total of 15 secondary-zone configurations within the 0.03 Å wide interval that we specified to define the transition state ensemble.

The same configurations were used for both hydride and deuteride shifts. The reaction coordinate,  $s_i$ , is calculated for the primary-zone atoms in mass-scaled coordinates (scaled to a reduced mass of 1 amu in all cases) by following the path of steepest descents in both directions from the saddle point for each secondary-zone configuration  $i$  ( $i = 1, 2, \dots, 15$ ). This path is isotope-dependent. The reaction path is calculated in the interval from  $R = -1.16$  to 1.16 Å for both isotopic cases. Note that because of the way in which  $s$  is mass scaled, this corresponds to moving farther downhill in the perprotio case than in the dideuterated case.

In Table 5, we show the SSZ (stage-2) average quasiclassical and tunneling transmission coefficients for both isotopes, as well as the overall transmission coefficients. The introduction of dynamical recrossing and quantum effects on the reaction coordinate for the hydride and deuteride transfers increases the KIE on  $k_2$  by a factor of 1.17 to 4.1. By including the equilibrium isotope effect on  $K_1$ , we obtain a total SSZ kinetic isotope effect of 4.4.

In Table 5, we have also given the root-mean-square deviation (rmsd) from the mean for all quantities. The 15  $\kappa_i^{\text{SSZ}}$  values for the hydride transfer exhibit a bimodal distribution with all values except for one falling into one of two groups, one group with

$1.2 < \kappa_i^{\text{SSZ}} < 1.9$  and another with  $\kappa_i^{\text{SSZ}}$  in the range of  $4.9 < \kappa_i^{\text{SSZ}} < 6.7$ . The only value of  $\kappa_i^{\text{SSZ}}$  that does not fall into one of these two groups is 2.7. This bimodal distribution gives rise to a large value for the rmsd. Note that the rmsd is not a measure of error or insufficient sampling; it does not tend to zero as the results are converged with respect to sampling. Rather it is presented as a characterization of the intrinsic width of the distribution. Because of the bimodal character, the rmsd divided by the mean is on the order of unity.

**2.5.4. Effects of Protein Environment on the Computed Kinetic Isotope Effect.** The static-secondary-zone approximation omits some of the effects of the thermal energy and entropy of the secondary-zone atoms. These effects are incorporated in the transmission coefficient determined using the equilibrium-secondary-zone (ESZ) approximation.<sup>18</sup> In this approximation, the primary zone atoms are held fixed along the reaction path from the SSZ calculation at a sequence of structures evenly spaced along the reaction coordinate  $s$ . For each of these structures we equilibrate the secondary-zone atoms by simulations of the full system to calculate the relative bath free energy as a function of  $s$ .

The ESZ approximation leads to an improved effective potential of mean force on the reaction path. Interpolations required for calculations of  $\kappa_i^{\text{ESZ}}$  were carried out with the VTST-ISPE-8 algorithm.<sup>57</sup> This method is a dual-level approach, where the fully converged reaction path is calculated at a lower level of theory (SSZ) and single-point energies are calculated at a higher level of theory (ESZ). A spline under tension is used to interpolate the difference of the ESZ single-point energies along the stage-2 minimum energy path and the SSZ energies (i.e.,  $V^{\text{ESZ/SSZ}} - V^{\text{SSZ}}$ ).

For ESZ calculations, we selected two of the 15 transition-state configurations. In particular, we selected the one with the largest  $\kappa_i^{\text{SSZ}}$  and the one with the smallest  $\kappa_i^{\text{SSZ}}$ . The SSZ KIE on  $k_2$  calculated using only these two configurations is 1.23 and is in acceptable agreement with the value of 1.17 calculated with the full ensemble of 15 configurations.

The relative bath free energies are calculated by free energy perturbation theory.<sup>53–56</sup> For the hydride transfer, we used nine windows at  $s = 0, \pm 0.29, \pm 0.58, \pm 0.87 \text{ \AA}$ , and  $\pm 1.16 \text{ \AA}$ . For each of these ESZ windows we ran 40 ps to equilibrate the system, followed by 30 ps of data collection, where we saved 300 configurations in each window for the free-energy calculation. We employed the double-wide sampling scheme<sup>53</sup> in which a sample at  $s = s_i$  was used to evaluate the perturbations at  $s = s_i \pm 0.5\Delta s$ , where  $\Delta s$  is the distance between windows. In the present case,  $\Delta s = 0.145 \text{ \AA}$  and the perturbation is acceptably small. For the deuteride transfer we should in principle redo the FEP calculations since the reaction paths are in principle different. However, the effect of the difference should be small for the present purpose, so it is reasonable to make the approximation that  $\Delta G_{\text{bath}}(s)$  depends only on  $z(s)$ , where  $z$  is defined in eq 1. We note that the  $z(s)$  function is different for the two isotopes, so we converted  $\Delta G_{\text{bath}}(s_{\text{H}})$  to  $\Delta G_{\text{bath}}(z)$  by using the  $z(s)$  function for H, and  $\Delta G_{\text{bath}}(z)$  was then converted to  $\Delta G_{\text{bath}}(s_{\text{D}})$  by using the  $z(s)$  function for D.

In the SSZ approximation, the free energy of the surrounding secondary zone is included in average way in the original 1D PMF used to calculate  $k^{(1)}$ , but the effect of bath relaxation along individual reaction paths is not included in  $\gamma^{(2)}$ . In the ESZ approximation, these effects are included in  $\gamma^{(3)}$ . In Figure 8, we show  $V_{\text{eff}}^{(\sigma)}$  as function of the reaction coordinate  $s$  for two trajectories for both  $\sigma = 2$  (SSZ) and  $\sigma = 3$  (ESZ). The figure clearly shows a large difference between the SSZ and ESZ

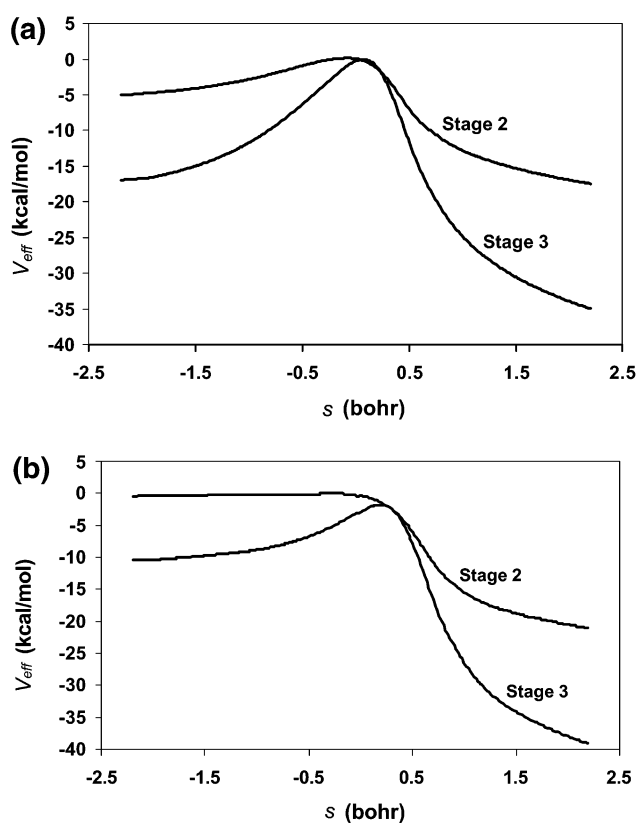


**Figure 8.** SSZ and ESZ effective potential  $V_{\text{eff}}^{(\sigma)}$  as functions of  $s$  for two of the configurations for the perprotio case.

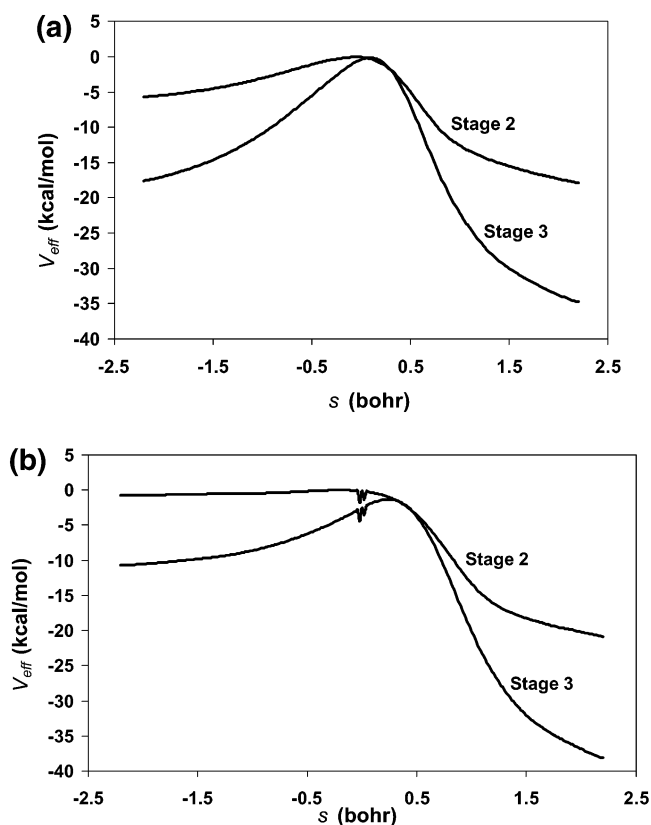


**Figure 9.** Same as Figure 8 but for the dideuterated case.

effective potentials; the ESZ barrier is steeper and narrower than the SSZ barrier. This change in shape gives rise to a much larger tunneling factor for the hydride transfer. In general, when there is large tunneling, the isotope effect is also large. Figure 9 shows

**TABLE 6: Computed Transmission Coefficients for the Protio and Deuterio Isotopes Using the Static-Secondary-Zone ( $\sigma = 2$ ) and Equilibrium-Secondary-Zone ( $\sigma = 3$ ) Approximation Averaged over Two Transition-State Configurations<sup>a</sup>**

isotope	$\Gamma^{(\sigma)}$	$\kappa^{(\sigma)}$	$\gamma^{(\sigma)}$
$\sigma = 2$			
HH	0.43(0.4)	3.9(3)	2.7(3)
DD	0.48(0.4)	3.3(2)	2.2(2)
$\sigma = 3$			
HH	0.86(0.04)	$3.2(3) \times 10^4$	$2.9(3) \times 10^4$
DD	0.82(0.10)	$1.5(1) \times 10^3$	$1.4(1) \times 10^3$

<sup>a</sup> Values in parentheses are root-mean-square deviations from the mean.

the corresponding dideuterated case. By comparing Figures 8 and 9, where both barriers are plotted in the same mass-scaled coordinate system, we see that barriers are steeper in the nonsubstituted case, which is consistent with the higher  $\kappa$  values for the reaction with the nonsubstituted substrate.

In Table 6, we show the ESZ average quasiclassical transmission coefficients for both isotopes. In this case, the introduction of quantum effects on the reaction coordinate for the hydride transfer increases the KIE by a factor of 20, whereas the corresponding SSZ value was only 1.17. Although we used 15 bath configurations for SSZ calculations, which provides a good sample, we used only two bath configurations in the latter (ESZ) study. So, these results have more statistical uncertainty. Nevertheless, inclusion of protein dynamical fluctuations in the reaction path calculation markedly increases the barrier height of the SSZ approximation, leading to enhanced tunneling effects. In Table 6, we have also included the corresponding SSZ values based on the smaller ensemble containing two configurations, and we note that these are in reasonable agreement with those obtained from the larger ensemble given in Table 5. Including the isotope effect on  $K_1$  as well as the effect of quantum mechanical vibrational zero-point energy gives a total ESZ kinetic isotope effect of 75.

**2.5.5. Overall Kinetic Isotope Effect.** In summary, the calculated total kinetic isotope effect is 4.4 in the SSZ approximation and 75 in the ESZ approximation. For comparison, the experimental value for the kinetic isotope effect is 6.9–17, depending on pH, from ref 3, and the KIE is 15, from ref 9, or it is 1.6–53, depending on the step, from ref 4. Reference 3 obtained 5.8 for deuterium substitution at C3, ref 4 obtained 15–53 for the second (slow) step, and ref 9 is consistent with an intrinsic KIE of 15–20 for MCAD with butyryl-CoA deuterated at C2 and C3; these values can be compared to our calculated value of 4.1 (SSZ) or 70 (ESZ) for the second (slow) step involving H<sup>−</sup> transfer from C3.

In the equilibrium-secondary-zone calculation, when the thermal energy and entropy of the secondary-zone atoms are included in the calculation of the transmission coefficients, the effective potential for primary zone dynamics is quite different from that with a static secondary zone. Thus, the large tunneling factors correspond to tunneling through a barrier of partly entropic (as opposed to energetic) origin; a large entropic contribution could cause the zero-order canonical mean-shape potential approximation to be unrealistic. The best estimate might lie somewhere between the SSZ frozen-bath results and the ESZ fully relaxed bath result, especially since the hydride transfer probably takes place on a faster time scale than the time scale of full relaxation of the bath. It may be necessary to allow the bath to relax but less than in the ESZ approximation where the extent of relaxation may be relatively overstabilizing the reactant and product states. We should also keep in mind

that the potential energy function represents a first attempt to model ACAD dynamics, and it is premature to draw conclusions about the dynamical models by comparison to experiment when we are uncertain about how possible errors in the potential function may affect the comparison.

### 3. Conclusion

This study explores the mechanism, reaction path, and kinetic isotope effect of the oxidation of butyryl-CoA to a *trans*-enoyl-CoA product in the active center of short-chain acyl-CoA dehydrogenase. By using a combined QM/MM simulation model and calculating a two-dimensional free energy surface, we have found that the reaction occurs in a stepwise manner with the hydride-transfer step having the dominant barrier. There is a dip in the free energy profile between the proton-transfer barrier and the hydride-transfer barrier, and this dip may be too small to have been observed. (Although in our calculation, the dip is deep enough for an intermediate to be observable, a somewhat smaller dip would be more consistent with experiment.) We then carried out a series of dynamical calculations that include quantum mechanical tunneling, quantized vibrational energy, and dynamical recrossing to determine the kinetic isotope effect on the reaction. The tunneling is treated with the canonical optimized multidimensional tunneling approximation, and the dynamical recrossing is estimated from the effective potential for each member of the transition state ensemble. The calculated static-secondary-zone KIE is smaller than the experimental value whereas the calculated equilibrium-secondary-zone KIE with the zero-order canonical mean-shape approximation for the effective potential is larger than the experimental value. The best estimate may lie between the SSZ and ESZ results. From one point of view it is discouraging that the SSZ and ESZ models show a large difference, but from another point of view it is encouraging because it means that the kinetic isotope effect carries useful sensitivity to details of the protein dynamics. Furthermore, it is encouraging that, in this first attempt to model ACAD dynamics, the two models we employed bracket the experimental value for the kinetic isotope effect.

**Acknowledgment.** The authors thank Marian T. Stankovich for helpful discussion, Ramkumar Rajamani for providing modifications of the CHARMM code, and Robert Bach, Olga Dmitrenko, Sandro Ghisla, and Colin Thorpe for helpful comments on the manuscript. This work was supported in part by the National Science Foundation (D.G.T.) under Grant No. CHE00-92019, by the National Institutes of Health (J.G.), and by a University of Minnesota Supercomputing Institute Research Scholarship to T.D.P., who also thanks Statens Naturvidenskabelige Forskningsråd for support. M.G.-V. is the recipient of a Fulbright Scholarship.

### References and Notes

- (1) (a) Fersht, A. *Enzyme Structure and Mechanism*, 2nd ed; Freeman: New York, 1985. (b) Blacklow, S. C.; Raines, R. T.; Lim, W. A.; Zamore P. D.; Knowles, J. R. *Biochemistry* **1988**, *27*, 1158–1167. (c) Cooper, A., Houben, J. L., Chien, L. C., Eds. *The Enzyme Catalysis Process*; Plenum: New York, 1989. (d) Davenport, R. C.; Bash, P. A.; Seaton, B. A.; Karplus M.; Petsko, G. A.; Ringe, D. *Biochemistry* **1991**, *30*, 5821–5826.
- (2) (a) Beinert, H. In *The Enzymes*; Boyer, P. D., Lardy, H., Mybäck, K., Eds.; Academic: New York, 1963; Vol. 7, pp 447–466. (b) Ghisla, S.; Engst, S.; Vock, P.; Kieweg, V.; Bross, P.; Nandy, A.; Rasched, I.; Strauss, A. W. In *Flavins and Flavoproteins*; Yagi, K., Ed.; de Gruyten: Berlin, 1994; pp 283–292. (c) Palfrey, B. A.; Massey, V. In *Comprehensive Biological Catalysis: A Mechanistic Reference*; Sinnott, M., Ed.; Academic: San Diego, CA, 1998; Vol. 3, pp 83–154.
- (3) Murfin, W. W. Mechanism of the Flavin Reduction Step in Acyl CoA Dehydrogenases. Ph.D. Thesis, Washington University, St. Louis, MO, 1974. Murfin, W. W.; Drysdale, G. Unpublished.
- (4) Reinsch, J.; Katz, A.; Wean, J.; Aprahamian, G.; McFarland, J. T. *J. Biol. Chem.* **1980**, *255*, 9093.



- (5) Raichle, T. Ph.D. Thesis, University of Konstanz, Konstanz, Federal Republic of Germany, 1981. Raichle, T.; Ghisla, S. Unpublished.
- (6) Ghisla, S.; Thorpe, C.; Massey, V. *Biochemistry* **1984**, *23*, 3154–3161.
- (7) Gorelick, R. J.; Schopfer, L. M.; Ballou, D. P.; Massey, V.; Thorpe, C. *Biochemistry* **1985**, *24*, 6830–6839.
- (8) Pohl, B.; Raichle, T.; Ghisla, S. *Eur. J. Biochem.* **1986**, *160*, 109–115.
- (9) Schopfer, L. M.; Massey, V.; Ghisla, S.; Thorpe, C. *Biochemistry* **1988**, *27*, 6599–6611.
- (10) Powell, P. J.; Thorpe, C. *Biochemistry* **1988**, *27*, 8022–8028.
- (11) (a) Johnson, J. K.; Srivastava, D. K. *Biochemistry* **1993**, *32*, 8004–8013. (b) Becker, D. F.; Fuchs, J. A.; Stankovich, M. T. *Biochemistry* **1994**, *33*, 7802–7087.
- (12) Shin, I.; Li, D.; Becker, D. F.; Stankovich, M. T.; Liu, H.-w. *J. Am. Chem. Soc.* **1994**, *116*, 8843–8844.
- (13) Nandy, A.; Kieweg, V.; Kräutle, F.-G.; Vock, P.; Küchler, B.; Bross, P.; Kim, J.-J. P.; Rasched, I.; Ghisla, S. *Biochemistry* **1996**, *35*, 12402–12411.
- (14) (a) Vock, P.; Engst, S.; Eder, M.; Ghisla, S. *Biochemistry* **1998**, *37*, 1848–1860. (b) Engst, S.; Vock, P.; Wang, M.; Kim, J.-J. P.; Ghisla, S. *Biochemistry* **1999**, *38*, 257.
- (15) (a) Peterson, K.; Galitz, D. S.; Srivastava, D. K. *Biochemistry* **1998**, *37*, 1697–1705. (b) Rudik, I.; Ghisla, S.; Thorpe, C. *Biochemistry* **1998**, *37*, 8437–8445. (c) Engst, S.; Vock, P.; Wang, M.; Kim, J.-J. P.; Ghisla, S. *Biochemistry* **1999**, *38*, 257–267. (d) Tamaoki, H.; Nishina, Y.; Shiga, K.; Miura, R. *J. Biochem. (Tokyo)* **1999**, *125*, 285–296. (e) Pellett, J. D.; Sabaj, K. M.; Stephens, A. W.; Bell, A. F.; Wu, J.; Tonge, P. J.; Stankovich, M. T. *Biochemistry* **2000**, *39*, 13982–13992. (f) Peterson, K. M.; Gopalan, K. V.; Nandy, A.; Srivastava, D. K. *Protein Sci.* **2001**, *10*, 1822–1834. (g) Gopalan, K. V.; Srivastava, D. K. *Biochemistry* **2002**, *41*, 4638–4648. (f) Lamm, T. R.; Kohls, T. D.; Stankovich, M. T. *Arch. Biochem. Biophys.* **2002**, *404*, 136–146.
- (16) Bach, R. D.; Thorpe, C.; Dmitrenko, O. *J. Phys. Chem. B* **2002**, *106*, 4325–4335. Bach et al. demonstrated that H-bonding interactions with the carbonyl group acidify the  $\alpha$ -proton and lower the activation barrier for proton transfer. After the present paper was submitted, they sent a new preprint (Dmitrenko, O.; Thorpe, C.; Bach, R. D. *J. Phys. Chem.* Submitted for publication) in which they find that a charge-transfer interaction between the developing thioenolate and the flavin also serves to activate this  $\alpha$ -proton.
- (17) Dewar, M. J. S.; Pierini, A. B. *J. Am. Chem. Soc.* **1984**, *106*, 203–208.
- (18) Alhambra, C.; Corchado, J. C.; Sánchez, M. L.; Garcia-Viloca, M.; Gao, J.; Truhlar, D. G. *J. Phys. Chem. B* **2001**, *105*, 11326–11340. Note the following correction to this reference: In eq 15,  $s = 0$  should be  $s = s_{0,j}$ .
- (19) Truhlar, D. G.; Gao, J.; Alhambra, C.; Garcia-Viloca, M.; Corchado, J. C.; Sánchez, M. L.; Villà, J. *Acc. Chem. Res.* **2002**, *35*, 341–349.
- (20) (a) Kumar, S.; Bouzida, D.; Swendsen, R. H.; Kollman, P. A.; Rosenberg, J. M. *J. Comput. Chem.* **1992**, *13*, 1011–1021. (b) Kumar, S.; Rosenberg, J. M.; Bouzida, D.; Swendsen, R. H.; Kollman, P. A. *J. Comput. Chem.* **1995**, *16*, 1339–1350. (c) Kumar, S.; Payne, P. W.; Vásquez, M. J. *Comput. Chem.* **1996**, *17*, 1269–1275.
- (21) Boczek, E. M.; Brooks, C. L., III. *J. Phys. Chem.* **1995**, *97*, 4509–4513.
- (22) Gao, J.; Xia, X. *J. Am. Chem. Soc.* **1993**, *115*, 9667–9675.
- (23) Martin, F. P.-D.; Dumas, R.; Field, M. J. *J. Am. Chem. Soc.* **2000**, *122*, 7688–7697.
- (24) (a) Calhoun, A.; Voth, G. A. *J. Chem. Phys.* **1998**, *109*, 4569–4575. (b) Crouzy, S.; Baudry, J.; Smith, J. C.; Roux, B. *J. Comput. Chem.* **1999**, *20*, 1664–1658. (c) Thomas, A.; Field, M. J. *J. Am. Chem. Soc.* **2002**, *124*, 12432–12438.
- (25) (a) Gao, J.; Amara, P.; Alhambra, C.; Field, M. J. *J. Phys. Chem. A* **1998**, *102*, 4714–4721. (b) Amara, P.; Field, M.; Alhambra, C.; Gao, J. *Theor. Chem. Acc.* **2000**, *104*, 336–343.
- (26) MacKerell, A. D., Jr.; Bashford, D.; Bellott, M.; Dunbrack, R. L., Jr.; Evanseck, J. D.; Field, M. J.; Fischer, S.; Gao, J.; Guo, H.; Ha, S.; Joseph-McCarthy, D.; Kuchnir, L.; Kuczera, K.; Lau, F. T. K.; Mattos, C.; Michnick, S.; Ngo, T.; Nguyen, D. T.; Prodhom, B.; Reiher, W. E., III; Roux, B.; Schlenkrich, M.; Smith, J. C.; Stote, R.; Straub, J.; Watanabe, M.; Wiórkiewicz-Kuczera, J.; Yin, D.; Karplus, M. *J. Phys. Chem. B* **1998**, *102*, 3586–3616.
- (27) Freindorf, M.; Gao, J. *J. Comput. Chem.* **1996**, *17*, 386–395.
- (28) Dewar, M. J. S.; Zebisch, E. G.; Healy, E. F.; Stewart, J. J. P. *J. Am. Chem. Soc.* **1985**, *107*, 3902–3909.
- (29) Hehre, W. J.; Radom, L.; Schleyer, P. V. R.; Pople, J. A. *Ab Initio Molecular Orbital Theory*; Wiley: New York, 1986.
- (30) Curtiss, L. A.; Raghavachari, K.; Redfern, P. C.; Rassolov, V.; Pople, J. A. *J. Chem. Phys.* **1998**, *109*, 7764–7776.
- (31) Frisch, M. J.; Trucks, G. W.; Schlegel, H. B.; Scuseria, G. E.; Robb, M. A.; Cheeseman, J. R.; Zakrzewski, V. G.; Montgomery, J. A.; Stratmann, R. E.; Burant, J. C.; Dapprich, S.; Millam, J. M.; Daniels, A. D.; Kudin, K. N.; Strain, M. C.; Farkas, O.; Tomasi, J.; Barone, V.; Cossi, M.; Cammi, R.; Mennucci, B.; Pomelli, C.; Adamo, C.; Clifford, S.; Ochterski, J.; Petersson, G. A.; Ayala, P. Y.; Cui, Q.; Morokuma, K.; Malick, D. K.; Rabuck, A. D.; Raghavachari, K.; Foresman, J. B.; Cioslowski, J.; Ortiz, J. V.; Stefanov, B. B.; Liu, G.; Liashenko, A.; Piskorz, P.; Komaromi, I.; Gomperts, R.; Martin, R. L.; Fox, D. J.; Keith, T.; Al-Laham, M. A.; Peng, C. Y.; Nanayakkara, A.; Gonzalez, C.; Challacombe, M.; Gill, P. M. W.; Johnson, B. G.; Chen, W.; Wong, M. W.; Andres, J. L.; Head-Gordon, M.; Replogle, E. S.; Pople, J. A. *Gaussian98 (Revision A.7)*; Gaussian, Inc.: Pittsburgh, PA, 1998.
- (32) Brooks, B. R.; Brucoleri, R. E.; Olafson, B. D.; States, D. J.; Swaminathan, S.; Karplus, M. *J. Comput. Chem.* **1983**, *2*, 187–217.
- (33) Gonzalez-Lafont, A.; Truong, T. N.; Truhlar, D. G. *J. Phys. Chem.* **1991**, *95*, 4618–4627.
- (34) Devi-Kesavan, L. S.; Garcia-Viloca, M.; Gao, J. *Theor. Chem. Acc.* **2003**, *109*, 133.
- (35) Curtiss, L. A.; Redfern, P. C.; Raghavachari, K.; Rassolov, V.; Pople, J. A. *J. Chem. Phys.* **1999**, *110*, 4703–4709.
- (36) (a) Gao, J.; Xia, X. *Science* **1992**, *258*, 631–635. (b) Gao, J. In *Modeling the Hydrogen Bond*; Smith, D. A., Ed.; ACS Symposium Series 569; American Chemical Society: Washington, DC, 1994; pp 8–21.
- (37) Djordjevic, S.; Pace, C. P.; Stankovich, M. T.; Kim, J.-J. P. *Biochemistry* **1995**, *34*, 2163–2173. Protein Data bank: 1BUC.
- (38) Thorpe, C.; Matthews, R. G.; Williams, C. H., Jr. *Biochemistry* **1979**, *18*, 331–337.
- (39) Allen, M. P.; Tildesley, D. J. *Computer Simulation of Liquids*; Oxford University Press: Oxford, U.K., 1987.
- (40) (a) Brooks, C. L., III; Brünger, A.; Karplus, M. *Biopolymers* **1985**, *24*, 843–865. (b) Brooks, C. L., III; Karplus, M. *J. Chem. Phys.* **1983**, *79*, 6312–6325.
- (41) Torrie, G. M.; Valleau, J. P. *Chem. Phys. Lett.* **1974**, *28*, 578–581.
- (42) Alhambra, C.; Wu, L.; Zhang, Z.-Y.; Gao, J. *J. Am. Chem. Soc.* **1998**, *120*, 3858–3866.
- (43) (a) Roux, B. *Comput. Phys. Commun.* **1995**, *91*, 275–282. (b) Beutler, T. C.; Bremi, T.; Ernst, R. R.; van Gunsteren, W. F. *J. Phys. Chem.* **1996**, *100*, 2637–2645. (c) Samuelson, S. O.; Martyna, G. J. *J. Chem. Phys.* **1998**, *109*, 11061–11073. (d) Samuelson, S. O.; Martyna, G. J. *J. Phys. Chem. B* **1999**, *103*, 1752–1766. (e) Bartels, C.; Schaefer, M.; Karplus, M. *J. Chem. Phys.* **1999**, *111*, 8048–8067. (f) Souaille, M.; Roux, B. *Comput. Phys. Commun.* **2001**, *135*, 40–57.
- (44) Daubner, S. C.; Gadda, G.; Valley, M. P.; Fitzpatrick, P. F. *Proc. Natl. Acad. Sci. U.S.A.* **2002**, *99*, 2702–2707.
- (45) Garcia-Viloca, M.; Alhambra, C.; Truhlar, D. G.; Gao, J. *J. Comput. Chem.* **2003**, *24*, 177–190.
- (46) Garcia-Viloca, M.; Alhambra, C.; Truhlar, D. G.; Gao, J. *J. Chem. Phys.* **2001**, *114*, 9953–9958.
- (47) (a) Garrett, B. C.; Truhlar, D. G. *J. Chem. Phys.* **1979**, *70*, 1593–1598. (b) Garrett, B. C.; Truhlar, D. G. *J. Am. Chem. Soc.* **1979**, *101*, 4534–4548.
- (48) Garrett, B. C.; Truhlar, D. G.; Grev, R. S.; Magnuson, A. W. *J. Phys. Chem.* **1980**, *84*, 1730–1748.
- (49) Schenter, G. K.; Garrett, B. C.; Truhlar, D. G. *J. Chem. Phys.*, in press.
- (50) Lu, D.-h.; Truong, T. N.; Melissas, V. S.; Lynch, G. C.; Liu, Y.-P.; Garrett, B. C.; Steckler, R.; Isaacson, A. D.; Rai, S. N.; Hancock, G. C.; Lauderdale, J. G.; Joseph, T.; Truhlar, D. G. *Comput. Phys. Commun.* **1992**, *71*, 235–262.
- (51) Truhlar, D. G.; Kuppermann, A. *J. Am. Chem. Soc.* **1971**, *93*, 1840–1851.
- (52) Truhlar, D. G.; Liu, Y.-P.; Schenter, G. K.; Garrett, B. C. *J. Phys. Chem.* **1994**, *98*, 8396–8405.
- (53) Jorgensen, W. L.; Ravimohan, C. *J. Chem. Phys.* **1985**, *83*, 3050–3054.
- (54) McCammon, J. A.; Harvey, S. C. *Dynamics of Proteins and Nucleic Acids*; Cambridge University Press: Cambridge, U.K., 1987.
- (55) *Computer Simulation of Biomolecular Systems*; van Gunsteren, W. F.; Weiner, P. K.; Wilkinson, A. J., Eds.; ESCOM: Leiden, The Netherlands, 1993; Vol. 2, pp 267–348.
- (56) Gao, J.; Kuczera, K.; Tidor, B.; Karplus, M. *Science* **1989**, *244*, 1069–1072.
- (57) Chuang, Y.-Y.; Corchado, J. C.; Truhlar, D. G. *J. Phys. Chem. A* **1997**, *103*, 1140–1149.
- (58) Truhlar, D. G.; Lu, D.-h.; Tucker, S. C.; Zhao, X. G.; González-Lafont, A.; Truong, T. N.; Maurice, D.; Liu, Y.-P.; G. C. Lynch, G. C. In *Isotope Effects in Chemical Reactions and Photodissociation Processes*; Kaye, J. A., Ed.; ACS Symposium Series 502; American Chemical Society: Washington, DC, 1992; pp 16–36.
- (59) Liu, Y.-P.; Lynch, G. C.; Truong, T. N.; Lu, D.-h.; Truhlar, D. G.; Garrett, B. C. *J. Am. Chem. Soc.* **1993**, *115*, 2408–2415.
- (60) Liu, Y.-P.; Lu, D.-h.; González-Lafont, A.; Truhlar, D. G.; Garrett, B. C. *J. Am. Chem. Soc.* **1993**, *115*, 7806–7817.
- (61) Fernandez-Ramos, A.; Truhlar, D. G. *J. Chem. Phys.* **2001**, *114*, 1491–1496.
- (62) Garcia-Viloca, M.; Alhambra, C.; Corchado, J. C.; Villà, J.; Gao, J.; Truhlar, D. G. CHARMMRATE version 2.0; a module of CHARMM version C28b3.